

A Comparative Study of Crystallography and Defect Structure of Corneal Nipple Array in *Daphnis nerii* Moth and *Papilio polytes* Butterfly Eye

Shamprasad Varija Raghu and R. Thamankar*



Cite This: *ACS Omega* 2020, 5, 23662–23671



Read Online

ACCESS |



Metrics & More

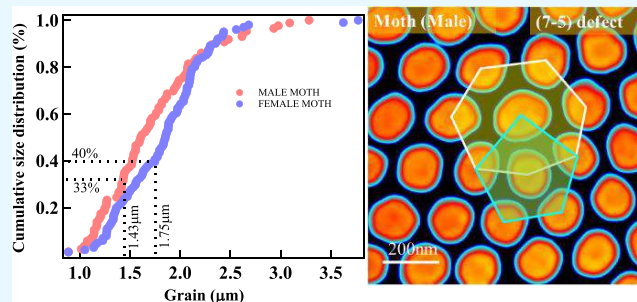


Article Recommendations



Supporting Information

ABSTRACT: Moth and butterfly ommatidial nanostructures have been extensively studied for their anti-reflective properties. Especially, from the point of view of sub-wavelength anti-reflection phenomena, the moth eye structures are the archetype example. Here, a comparative analysis of corneal nipples in moth eye (both Male and Female) and butterfly eye (both Male and Female) is given. The surface of moth (Male and Female) and butterfly (Male and Female) eye is defined with regularly arranged hexagonal facets filled with corneal nipples. A detailed analysis using high-resolution scanning electron microscopy images show the intricate hexagonal arrangement of corneal nipples within the individual hexagonal facet. Individual nipples in moth are circular with an average diameter of about 140/165 nm (Male/Female) and average internipple separation of 165 nm. The moth eye show the ordered arrangement of the corneal nipples and the butterfly eye (Male/Female) show an even more complex arrangement of the nipples. Structurally, the corneal nipples in both male and female butterflies are not circular but are polygons with 5, 6, and 7 sides. The average center-to-center separation in the butterfly (Male/Female) is about 260 nm/204 nm, respectively. We find that these corneal nipples are organized into much more dense hexagonal packing with the internipple (edge-to-edge) separation ranging from 20 to 25 nm. Each hexagonal facet is divided into multiple grains separated by boundaries spanning one or two crystallographic defects. These defects are seen in both moth and butterfly. These are typical 5-coordinated and 7-coordinated defect sites typical for a solid-state material with the hexagonal atomic arrangement. Even though the isolated defects are a rarity, interwoven (7-5) defects form a grain boundary between perfectly ordered grains. These defects introduce a low-angle dislocation, and a detailed analysis of the defects is done. The butterfly eye (Male/Female) is defined with extremely high-density corneal nipple with no apparent grains. Each corneal nipple is a polygon with “ n ” sides ($n = 5, 6, \text{ and } 7$). While the 5- and 7-coordinated defects exist, they do not initiate a grain rotation as seen in the moth eyes. To find out the similarity and the difference in the reflectivity of these nanostructured surfaces, we used the effective medium theory and calculated the reflectivity in moth and butterfly eyes. From this simple analysis, we find that females have better anti-reflective properties compared to the males in both moth and butterfly.



INTRODUCTION

Nature has been an inspiration for humans since centuries. Various structures available as a creation of nature surprise us even today. For example, the colors exhibited by the butterfly wings are a subject of intense curiosity and research studies for few decades.^{1–7} They have caught the eyes of humans by surprise due to the variety of colors exhibited by the wings. Another important aspect is the design of their eyes with minimum reflection and also enables them to reflect ultraviolet and polarized light.^{8,9} One of the earliest experimental works done on the classification of insect species based on nipple height and arrangement showed that the nipples are hexagonally arranged with height variation between 50 and 250 μm. This study suggested that the varied height of corneal nipples in different species indicate the evolutionary development and diversification.¹⁰ Hexagonal arrays on cicada (e.g.,

Psaltoda claripennis) and termite (e.g., family Rhinotermitidae) wings have been investigated. The study reveals that the structures have spacings that vary between 200 and 1000 nm with rounded shape protruding out about 150–350 nm from the surface.¹¹ Recently, the scanning electron microscopy study on the corneal nipple nanostructures of diurnal butterfly species indicated more intricate hexagonal packing with multiple domains. Here also, the spacing between the nipples ranged between 180 and 240 nm and the height varied

Received: May 18, 2020
Accepted: August 25, 2020
Published: September 9, 2020



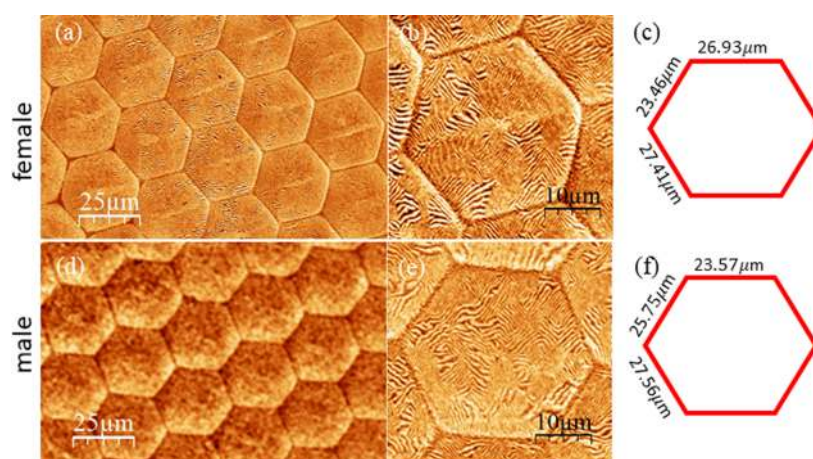


Figure 1. Scanning electron microscopy (SEM) images of the eye in female and male moth (top and bottom row, respectively). (a, d) Typical large-scale image of the eye showing regular facets with hexagonal symmetry. (b, e) Single hexagonal facet. Scale bars, 10 μm . By performing a Fourier transform of these topographical images, the average sizes of the hexagon are determined and shown in (c) and (f). The average area of each hexagonal facet is 1747 μm^2 for female and 1705 μm^2 for male.

between 0 nm (papilionids) and 230 nm (nymphalid).¹² It has been assumed that both the butterflies and moths have color vision and the precise method of color vision is not fully understood yet. In this regard, extensive research has been undertaken to understand the moth eye structure, image formation, and image processing in the eyes of butterflies and moths.^{12–14} To understand the function of these corneal nipples, several theories have been put forward. The most commonly used theory indicates the reduced reflection of light by the corneal nipples, thereby increasing the amount of light captured.¹⁵ Another theory suggests that these corneal nipple arrays reduce the eye glare, thus saving themselves from the predator.¹² It is also suggested that the moth eyes are evolved in such a way that the nanostructured corneal nipple array reduces the adhesion due to a reduction in the contact area of contaminating particles.¹⁶ Since there is no correlation between the type of nanostructure and the evolutionary stage of the group, the various categories belong to a diverse set of Turing patterns.¹³

The anti-reflection properties have been studied by coating nanostructured materials on surfaces (both hard and flexible) and understanding the absorption and transmission properties of these coatings.^{17–26} The tiled sub-wavelength nanostructures also reduce the iridescence caused by the diffraction of light incident at high angles.²⁷ This phenomenon is modeled by considering different shapes of nipples (pillars, parabola, and cones).^{28,29} Recently, by employing self-assembly of polymer and then plasma etching, scientists have fabricated moth eye structures to enhance the broadband anti-reflection in silicon solar cells.³⁰ Such sub-wavelength nanostructures will show broadband anti-reflection over a wide angle of incidence when the height is more than $\sim 0.4\lambda$ and spacing $l \approx \lambda/2n_s$, where n_s is the refractive index of the substrate.³¹ Currently, the material nanostructures can be precisely controlled by means of fast-improving nanofabrication techniques. Better anti-reflective structures have paved the way for advanced manufacturing of moth-eye structures for various applications such as solar cells,³² light-emitting diodes,³³ and display screens.³⁴ In this direction, the analysis of chitin nanostructure in the eyes of butterflies and moths needs to be understood in detail.^{35–38}

In the case of moths and butterflies, moths are active in the night (nocturnal) and the butterfly is active during the day time (diurnal). Even though both come under the same order *Lepidoptera*, their activity is completely different. We set out to see the similarities/differences and to understand the optical reflectivity of the nanostructured eyes of a particular species of moth (*Daphnis nerii*) and a butterfly (*Papilio polytes*), which are available across India and Asia. In this paper, we will give a detailed structural analysis of chitin nanonipples in the eyes of *Daphnis nerii* moths and *Papilio polytes* butterfly.

We analyzed the scanning electron microscopy images of corneal nipples in moths (Male/Female) and butterflies (Male/Female). We find that the eye is divided into multiple hexagonal facets. In the case of moth (Male/Female), the corneal nipples are arranged in a hexagonal arrangement. A comparison is made between the size and separation between the moth and butterfly. The hexagonal arrangement is not perfect, extending to large distances. Each facet is divided into small areas of a perfect hexagonal arrangement separated by single or a combination of defects forming a grain boundary.³⁷ The formation of such defects or linear defects is compared to the solid-state materials like graphene^{39–41} and h-BN,^{42–44} which also contain a hexagonal arrangement of atoms.

RESULTS AND DISCUSSION

Figure 1a,d shows a low-magnification scanning electron microscopy (SEM) images of moth (Female and Male) eyes. The top row is from the female eye, and the bottom row is from the male eye. Both eyes are characterized by a very dense hexagonal facet structure. Individual hexagonal facet is shown in (b) and (e). We take the Fourier transform of the large-area images to calculate the size of individual hexagonal facets, and the sizes of each hexagonal structure are schematically shown in (c) and (f) for female and male, respectively. We find that each hexagon is not exactly identical and varies in size. The average area of each hexagonal facet is 1747 μm^2 for female and 1705 μm^2 for male. On average, we see that the area of individual hexagonal facet for a female moth is larger than a male moth by 2–3%. Additionally, at some locations where two hexagonal facets join, we see antenna-like protrusions with large aspect ratio, with no periodicity. At this juncture, it is not clear what are the functions of these protrusions.

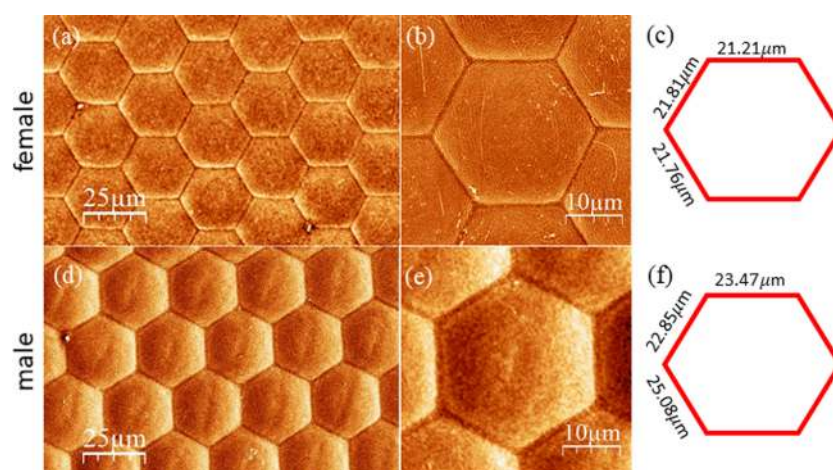


Figure 2. Scanning electron microscopy images of the eye of female butterfly and male butterfly (top and bottom row, respectively). (a, d) Typical large-scale image showing facets with hexagonal symmetry. (b, e) Single hexagonal facet. In both images, the scale bar is set to $10 \mu\text{m}$ so that the sizes can be compared. Fourier transform of the topographical images gives the average sizes of the hexagonal facets shown in (c) and (f). The average area of each hexagonal facet is $1211 \mu\text{m}^2$ for females and $1509 \mu\text{m}^2$ for males.

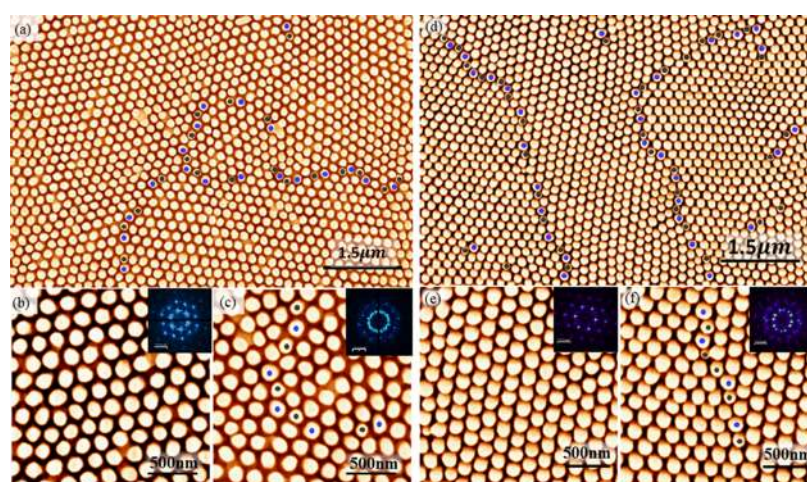


Figure 3. Scanning electron micrograph of the eye of a moth (Male) within one hexagonal facet. (a) Small area within a single hexagonal facet showing the nipple organization in hexagonal packing with multiple grains. The black and blue dots represent the 5- and 7-coordinated defects, respectively. Grain boundaries are defined by single or line defects. The image size is $7.5 \mu\text{m} \times 5.6 \mu\text{m}$; scale bar, $1.5 \mu\text{m}$. Small-area scan within the grain is shown in (b). The nipple arrangement is very regular within the grain further supported by the Fourier transform image in the inset. The grain boundary region is shown in (c). The Fourier transform shows more than one grain, indicating the rotation across the boundary. The scan area is $2 \mu\text{m} \times 2 \mu\text{m}$; scale bar, 500 nm . (d) Image of moth (Female) eye within one hexagonal facet. The whole area is divided into multiple grains separated by grain boundary represented by 5-coordinated (black) and 7-coordinated (blue) defects. The image size is $7.5 \mu\text{m} \times 5.6 \mu\text{m}$. Small-area scans within the grain and grain boundary region are shown in (e) and (f). The pillar arrangement is very regular within the grain supported by the Fourier transform image in the inset. Scale bar, $7.9 \mu\text{m}^{-1}$. The area near to a grain boundary shown in (f), and the Fourier transform show two grains rotated with respect to each other by 19° . The scan area is $2 \mu\text{m} \times 2 \mu\text{m}$; scale bar, $7.9 \mu\text{m}^{-1}$.

Similar hexagonal facets can be seen in butterfly male and female as shown in Figure 2a,b. The butterfly eye is also characterized by high-density hexagonal facets. The individual facets as shown in Figure 2b,d indicate that these are more regular with similar side lengths. The average dimensions of these hexagonal facets can be calculated by Fourier transform of the large-area images. Figure 2c and Figure 2f represent the schematic of the dimensions of the individual facets for butterfly females and males, respectively. The average area of each hexagonal facet is $1211 \mu\text{m}^2$ for females and $1509 \mu\text{m}^2$ for males. In the case of the butterfly, the average area of hexagonal facet of male butterfly is 20% larger than that of female butterfly. This is exactly opposite to the case in moth (Male/Female).

Analysis of Moth Eyes. There are interesting features within the individual hexagonal facet of moth eyes. It is divided into multiple grains of no particular defined area. A small region within one facet of the moth (Male) eye is shown in Figure 3a. This contains few grains where corneal nipples maintain the hexagonal symmetry. We use a similar approach to analyze the high-resolution electron microscopy images as adopted in the case of Mourning Cloak butterfly eye.^{35–37} Each nipple can be imagined as a 6-coordinated site. The individual grain extends up to about 20–30 lattice sites and are separated by one or two distorted nipple arrangement resulting in a (7-5) defect site. The transition from grain to grain occurs at a 5-coordinated site (black dot) or a 7-coordinated site (blue dot). These are defects commonly observed in eyes of

both male and female moth. Figure 3b shows a typical region within the grain where nipples have a hexagonal symmetry or 6-coordination. The inset shows a Fourier transform image and indicates a perfect hexagonal arrangement of corneal nipples. At the same time, if one looks at the grain boundary region as in Figure 3c, there is a (7-5) defect and around which the grain orientation changes. The Fourier transform in the inset also shows a complex hexagonal symmetry of three grains rotated with respect to each other by 17° , 22° , and 23° . We used the Fourier transform images to calculate the nearest neighbor separation (the detailed analysis of the Fourier transform images are given in Figure S1 in the Supporting Information). A similar analysis of the nipple arrangement within a single facet of the moth (Female) reveals rich crystallographic features. Again, the facet is divided into multiple grains with no defined grain area as shown in Figure 3d. The nipples are arranged in the hexagonal arrangement within an individual grain. The grain boundaries are defined with 5-coordinated (black dot) or 7-coordinated defect (blue dot) or one or two (7-5) defects.

A small area with a perfect hexagonal arrangement of pillars is shown in Figure 3e. The Fourier transform suggests a perfect hexagonal symmetry as shown in the inset. A detailed analysis of the images from various locations indicates that the rotation of grains starts at the (7-5) defect. Grains are rotated by well-defined angles with respect to each other across grain boundaries. As shown in Figure 3f, the grain rotation originates at a (7-5) defect and boundaries span a few 7-coordinated or 5-coordinated defect sites. In this particular case of Figure 3f, there are two (7-5) defects side-by-side and the grain on the left and right are rotated by an angle of 23° . This is also revealed by the Fourier transform image showing two hexagonal grains rotated by 23° . The details of the Fourier transform images are explained in detail in the Supporting Information. A detailed analysis is shown in Figure S2 in the Supporting Information.

To get a clear idea about the angular rotation of grains, we analyzed a small area near to a grain boundary for moth (Male). Care is taken to consider an area quite far from the edge of the facet. As indicated in Figure 4a, the grain boundary clearly originates from a 5-coordinated defect shown in the center. The grain boundary also consists of a series of (7-5) defects with no particular position dependence. The boundary is defined by interconnected 5- and 7-coordinated defects or interconnected (7-5) defects. The angular separation between the individual grains across the boundary is about 30° . The high angle of misorientation between the grains could be due to the close packing of the (7-5) defects as seen along the boundary. A similar large-angle misorientation was observed in the case of the Mourning Cloak butterfly eye.³⁶ Some of the (7-5) defects are rotated by $12\text{--}15^\circ$ with respect to each other. These defects combine themselves to form low-angle grain boundaries. The occurrence of such low-angle grain boundaries is similar to the case of grain boundaries in solid-state materials like graphene and h-BN.^{42,45}

The presence of a low-angle ($\theta < 15^\circ$) and a high-angle ($\theta > 15^\circ$) misorientation can be explained using two models used in the solid-state structures. The high-angle boundaries can be explained using a model such as a structural unit model.^{46,47} A low-density uniform distribution of the (7-5) defects results in low-angle boundaries, and a high-density uniform distribution will yield a high-angle boundary. In our case, we have observed high-angle boundaries with angle or

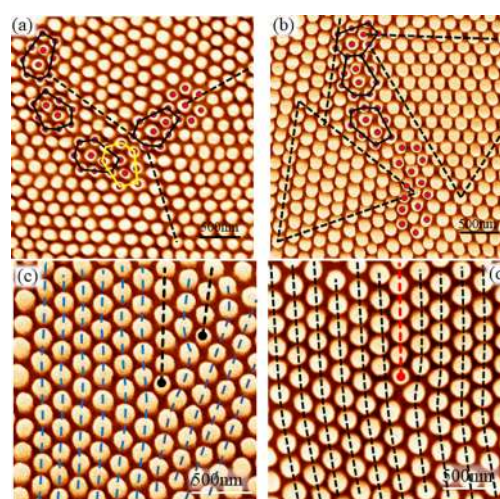


Figure 4. Defect structures in moth (Male/Female) eye. (a) The otherwise ideal hexagonal lattice includes a defect with 7-coordination site and a 5 coordination site constituting a (7-5) defect as shown by the distorted hexagon in yellow. The grain boundary region is filled with these (7-5) defects. On a few occasions, there is an isolated 7-coordinated site as shown on the right side. (b) (7-5) defect structure along the grain boundary in the moth (Female) eye. The dashed triangles represent perfect hexagonal grains. There are a series of 5-coordinated sites separating the adjacent grains. These defect locations also mark the grain boundaries. The dashed lines are guide to the eye. The scan area is $3 \mu\text{m} \times 3 \mu\text{m}$. The scale bar is 500 nm in both cases. (c, d) Dislocations in the nanonipple structure of moth (Male/Female). (c) Two such dislocations starting at the 5-coordinated defect indicated by the black dashed line. The normal hexagonally organized nipples are also indicated by blue dashed lines. Similarly, in the case of moth (Female), there is a dislocation starting at the 5-coordinated site. The low-angle dislocations can be seen in the male and female moth eye starting at the 5-coordinated site. The average distance of separation between the 5-coordinated sites in males and females is 839 and 727 nm, respectively. The scan area is $2 \mu\text{m} \times 2 \mu\text{m}$; scale bars, 500 nm.

misorientations of 23° and 30° . In the case of moth (Female) as shown in Figure 4b, the misorientation is about 30° between the two single-crystal grain regions marked by the dashed lines. In this case, the grain boundary is filled with more number of interconnected (7-5) defects. The boundary also shows a (5-7-5) defects and individual 5-coordinated defect. A similar distribution of angle of misorientation is normally found in the solid-state materials with hexagonal atomic arrangements such as single-wall carbon nanotubes.³⁹ A recent study on single-wall carbon nanotubes with similar hexagonal arrangements suggests that the grain boundaries due to (7-5) defects can be formed with misorientation angles of $(0^\circ, 21.79^\circ)$, $(42.1^\circ, 60^\circ)$.⁴¹ Due to the misorientation, the large strain is developed in the lattice, and for a 30° misorientation, the strain energy is minimum. Our analysis of the misorientation angles in the pillar arrays matches very well with the solid-state materials like a single wall carbon nanotube. Even in the case of the heteroatomic system like hexagonal boron nitride (h-BN), a similar distribution of misorientation can be seen with grain boundaries made of (7-5) giving less strain.^{42,44} Even though the defect size found here is two orders of magnitude large compared to the atomic scale defects found in graphene or h-BN, we expect a similar straining effect on the surface of the eyes due to the curvature. With these well-defined angles of misorientation, the structure also minimizes its strain energy by

having a line of these defects forming the grain boundaries. In the case of low misorientation angles ($\theta < 15^\circ$) in solid-state nanostructures of a similar kind, a dislocation model has been used.

According to this model, the angle of misorientation can be found as $\theta = \frac{x}{y}$ by measuring the nearest neighbor distance x and the average separation between the 5-coordinated site, which can be considered as Burgers vector y .^{37,48} In the case of moth(Male), the average nearest neighbor distance is 166 nm and the average distance between the 5-coordinated site is about 839 nm. Then, the angle of misorientation is 11.2° , which is fairly close to the angle 12° measured using the Fourier transform of the image near to the grain boundary. A similar calculation for the moth(Female) gives a misorientation angle 12.8° (the nearest neighbor distance is 165.8 nm, and the average distance between the 5-coordinated defect is about 727 nm), which agrees very well with the misorientation angle measured from the images. In order to see if there are low-angle boundaries, we checked for dislocations in the images. We made sure that the location analyzed is far from the facet edges. Figure 4c and Figure 4d show a low-angle dislocation in a moth(Male/Female), respectively. The close-packed nipple arrays are marked with dashed lines. An extra row of nipples starts at a 5-coordinated defect as shown with a black dashed line. Figure 4c shows two of such 5-coordinated sites where an extra row of nipple array starts. We call this as dislocation as per the definitions of solid-state crystallography. Similarly, in the case of moth(Female), an extra row of nipple array starts at the 5-coordinated defect as shown in Figure 4d by red dashed line.

We have investigated both moth(Male) and moth(Female) in great detail, and the results are summarized in Table 1. We

Table 1. Overview of Image Analysis

characteristics	moth		butterfly	
	Male	Female	Male	female
diameter of the nipple as seen in SEM (nm)	140	165	190	215
average separation (nm)	166	166	260	284
low-angle dislocation (in degrees)	9.4	11.46	12.82	12.95

take different regions of the hexagonal arrangement of nipples and by Fourier transforming these images to get average separation between the nipples. In the case of both moth(Male) and moth(Female), the average separation between the nipples is about 166 nm as shown in Figure 3. In fact, we see anisotropic distribution of separation along three directions considered from the point of intersection of the hexagonal facets. This anisotropy of the separation can be attributed to the curvature of the eye and also imaging by scanning using an electron microscope. From the particle analysis, we find that the individual nipple varies in dimension. Assuming they are circular as seen from the electron microscope, the average diameter of the pillar in a moth(Male) and moth(Female) is 140 and 165 nm, respectively. It is important to note that, in both parameters, the individual size and separation are in the sub-optical regime (less than 400 nm). It is clear from Table 1 that the corneal nipples in the case of a butterfly(Male/Female) are bigger in size compared to a moth. Since the individual nipples are bigger in butterfly, the corresponding interpillar distance is large. The higher

density of the pillar arrangement in butterfly acts to a disadvantage in terms of the anti-reflective properties. If one compares the reflectance of the butterfly and the moths, the moths fare much better compared to the butterfly. It is possible that the higher density of the pillar arrangement is not really essential to reduce the reflection of light but an optimal $\frac{a_p}{a_{\text{hex}}}$ is needed. Here, one needs to remember that the moths are nocturnal and the butterfly is diurnal. Our analysis is purely based on the crystallographic structure of the eye. Similar measurements have been done for various butterfly species like *Papilionidae*, *Pieridae*, *Lycaenidae*, etc.,¹² and our analysis match very well.

Our results also show random nucleation and growth of the nipples, which eventually show up as grains with the regular arrangement. The areas of perfect hexagonal arrangement was noted down using ImageJ software for each grain and noted down the area. The misorientation of two adjacent grains start at a 5-coordinated defect. We took such 5-coordinated sites as a reference to mark the grain boundary. ImageJ calculates the area of the user-defined shapes. The area of various grains show log-normal distribution in both moth(Male/Female). The average grain size in a moth(Male) is $1.43 \mu\text{m}$. The cumulative size distribution shows that only 33% of grains are equal to or less than $1.43 \mu\text{m}$. This also implies that the majority of the grains are in the small size distribution range between 1 and $2 \mu\text{m}$. In the case of moth(Female), the average grain size is about $1.75 \mu\text{m}$. In this case, about 40% grains equal to or less than $1.75 \mu\text{m}$. The majority of grains are within $1.3\text{--}2.3 \mu\text{m}$. From this analysis, it is clear that the average grain size in the moth(Female) is larger by about 20–25% compared to males. The grain size and cumulative size distribution for both moths(Male/Female) are shown in Figure S3 in the Supporting Information. Our analysis on grain size distribution of the male *Daphnis nerii* eye compares well with the Mourning Cloak butterfly eye,³⁶ while the average grain size of the female *Daphnis nerii* eye is larger.

Such sub-wavelength nanostructures have been taken as a reference for designing highly efficient anti-reflective coating in recent years. For instance, a close-packed polystyrene nanosphere monolayer with extremely high transmittance has been designed on this principle. Assuming a parabolic shape of these individual nipples results in a linear variation of the refractive index, which effectively reduces the reflectance at the surface.⁴⁹ Polyethylene terephthalate (PET) coated with TiO_2 nanoparticles show up excellent transmittance to 90% in the optical region (400–700 nm).⁵⁰ Similarly, the biomimetic nanostructures fabricated on polycarbonate substrates using nanoimprint lithography (NIL) showed excellent (99%) anti-reflective properties.⁵¹ Based on these fabricated nanostructures, we assume that the moth considered here also have an extremely good anti-reflective property in the optical wavelength regime.

To understand the anti-reflective property of the moth(Male) and moth(Female) eyes, we adopt the much-discussed effective medium theory (EMT).⁵² If the nipple is tapered, then the fraction of material increases toward the base and correspondingly the refractive index will also change. This gradual change in the refractive index ensures that light does not experience an abrupt change in the refractive index, which might cause a large amount of light to be reflected. This will result in better anti-reflective property in the wide wavelength range. The difference in the average diameter of the individual nipples ultimately results in different area density in a

moth(Male) compared to a moth(Female). Since the average interpillar separation and size of the individual pillar are smaller than the wavelength of optical light, we can use the effective medium theory to understand the anti-reflection mechanism. In this scenario, propagation of light is explained using an effective refractive index (n_{eff}), which can be calculated using the effective medium theory (EMT):^{12,49}

$$n_{\text{eff}} = [f \cdot n_p^{2/3} + (1 - f) \cdot n_0^{2/3}]^{3/2} \quad (1)$$

where n_{eff} is the effective refractive index, and f is the fill factor for the hexagonal lattice structure in the eye. We take the refractive index of the nipple (n_p , made of chitin) as 1.52 and n_0 equal to 1.00. This means that the effective refractive index strongly depends on the fill factor f of the hexagonal lattice. We can make use of the classical optics to evaluate the fill factor of this open hexagon using the equation

$$f = \frac{A_p}{A_{\text{hex}}} = \frac{\pi r_p^2}{\sqrt{3} a_{\text{hex}}^2} = \frac{\pi}{2\sqrt{3}} \left(\frac{a_p}{a_{\text{hex}}} \right)^{3/2} \quad (2)$$

where a_p and a_{hex} are the average diameter of an individual nipple and the average distance of separation of nipples in the hexagonal lattice, respectively. We find the fill factors of 0.644 and 0.842 with effective refractive indices of 1.327 and 1.429 for moth(Male) and moth(Female), respectively. The reflectance can be calculated for the sub-wavelength pillar arrangement using Fresnel's equation:

$$R(\%) = \left(\frac{n_{\text{eff}} - n_b}{n_{\text{eff}} + n_b} \right)^2 \quad (3)$$

where $R(\%)$ is the calculated values of reflectance, and n_b is the refractive index of the base material. The dependence of the reflectance with the refractive index of the base material can be computed and is shown in Figure 5a. We see quite a dramatic

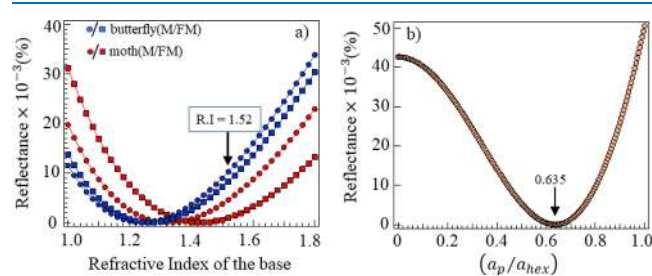


Figure 5. (a) Calculated reflectance against the refractive index of the base material. The red and blue data points are for moth and butterfly, respectively. The arrow indicated by R.I = 1.52 indicates that of the chitin material, which supports the corneal nipples in the eyes. Overall reflectance of the butterfly is more than moths. Comparative plots between the male (moth/butterfly) and female (moth/butterfly) are shown in Figure S4 in the Supporting Information. (b) Reflectance as a function of $\frac{a_p}{a_{\text{hex}}}$. Here, a_p and a_{hex} are the internipple separation and the side length of the hexagonal arrangement, respectively. The minimum occurs at a ratio of 0.635.

difference in the reflectivity between the male and female moths. Taking chitin (with R.I. \approx 1.52) as the base material, we see that the female moth eye has lesser reflectance compared to the male moth by almost two orders of magnitude. This implies that it is highly probable that female moths will survive better than the male moth. A similar

calculation can be done for butterfly, and we find that the reflectance from the male butterfly is an order of magnitude higher compared to that from the female butterfly. Again, here also the female butterfly is likely to survive more compared to the male butterfly from predators.

The reflectance ($R(\%)$) can also be written as a function of the $\frac{a_p}{a_{\text{hex}}}$ written as

$$R(\%) = \left[\frac{\left(0.793 \left(\frac{a_p}{a_{\text{hex}}} \right)^2 + 1 \right)^{3/2} - 1.52}{\left(0.793 \left(\frac{a_p}{a_{\text{hex}}} \right)^2 + 1 \right)^{3/2} + 1.52} \right]^2 \quad (4)$$

where we have taken the chitin as the base material ($n_b = 1.52$). The above equation is under the assumption of a perfect hexagonal pillar arrangement and a flat surface. This is a good approximation since the hexagonal facets span an area more than $1250 \mu\text{m}^2$. Here, we restrict our interest to $\frac{a_p}{a_{\text{hex}}} = 1$ as this correspond to the nipples touching each other.

As shown in Figure 5b, the reflectance has minimum when the ratio $\frac{a_p}{a_{\text{hex}}} = 0.635$. From the electron microscopy images, this ratio for moth(Male/Female) is 0.843/0.99 and that for butterfly(Male/Female) is 0.730/0.757. This means that the corneal nipples arranged hexagonally still far away from the optimal design such that there is almost no reflectance of the light. If we compare the male moth and male butterfly, moth eyes have evolved to give lesser reflectance compared to the butterfly. More detailed dependence of reflectance with refractive index of the base material is shown in Figure S4 in the Supporting Information.

Analysis of Butterfly Eyes. A similar analysis of the corneal nipples within the individual facet of butterfly(Male) and butterfly(Female) shows quite a different pillar arrangement. On a large scale, the nipples are organized in the form of hexagonal facets, but if one looks into details within the facet, there are two distinct differences compared to moth eyes. As shown in Figure 6a,d, individual facet reveals a very dense arrangement of the nipples, which have regular shapes (polygons) as seen in the high-magnification electron microscopy images. The overall pillar arrangement consists of either 5-sided, 6-sided, or 7-sided corneal nipples. The majority of the nipples are hexagonal in shape (6-sided) having six nearest neighbors forming an ideal hexagonal arrangement. These six nearest neighbors will be either 5-sided, 6-sided, or sometimes even 7-sided corneal pillar. While the corneal nipples in moth(Male/Female) eyes are well separated, the butterfly corneal nipples are densely packed such that the average separation between the individual nipple is extremely small (between 22 and 25 nm). The Fourier transform indicates more of an amorphous organization of the corneal nipples. The area is not divided into grains, and both male and female butterflies show similar characteristics. The exact reason for this kind of amorphous-like nipple arrangement and how this affects the detection process is not known. A very high-resolution image shown in Figure 6c show a 7-coordinated defect indicated by the blue dot. This 7-coordinated defect is in complete contrast to the 7-coordinated defect in moth eyes. The central nipple itself is a heptagon (7-sided polygon), which is surrounded with seven more nipples. In this particular case, two pentagonal nipples (2P) and five hexagonal nipples

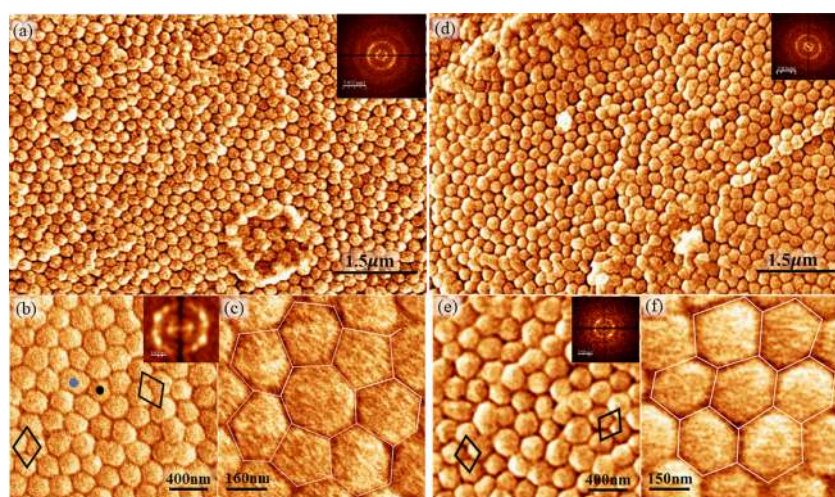


Figure 6. Scanning electron microscopy image of the butterfly (Male/Female) eye inside a hexagonal facet. (a) Large-scale image showing very high-density packing of the corneal nipples in the butterfly (Male) inside the single hexagonal facet. All the corneal nipples are polygons (5-, 6-, 7-sided polygons). The Fourier transform does not show any bright diffraction spots, indicating that there are no ordered grains. The scan size is $7.5 \mu\text{m} \times 5.6 \mu\text{m}$ with a scale bar of $1.5 \mu\text{m}$. (b) Small-area scan showing a hexagonal arrangement. Black and blue dots indicate a 5- and 7-coordinated defect combining into a (7-5) defect. The Fourier transform shows a local order with unit cells in two directions as indicated. The scan area is $2.1 \mu\text{m} \times 2.1 \mu\text{m}$. (c) Single 7-coordinated defect. The pillars are of polygons with a number of sides varying from 5 to 7. The scan area is $0.81 \mu\text{m} \times 0.77 \mu\text{m}$. In this case, there are two pentagons and five hexagons surrounding a central pillar with 7-sides. (d) Large-area scanning electron microscopy image of the butterfly (Female) eye inside a single hexagonal facet. The diffused Fourier transform pattern indicated an amorphous organization of the pillars. The scan size is $7.5 \mu\text{m} \times 5.6 \mu\text{m}$ with a scale bar of $1.5 \mu\text{m}$. (e) Very dense hexagonal packing combined with the 5- and 7-coordinated defect. The scan area is $2.1 \mu\text{m} \times 2.1 \mu\text{m}$. (f) Hexagonally arranged cell with all the nipples being hexagonal. The scan area is $0.81 \mu\text{m} \times 0.77 \mu\text{m}$.

(5H) make the 7-coordinated 2P-5H defect. Careful observation of the high-resolution images reveals that there is no 2P-5H arrangement requirement among all the 7-coordinated defects. Near to the 7-coordinated defect, there is a 5-coordinated defect indicated by the black dot. The combination of a 5- and 7-coordinated defect forms a (7-5) defect.

Similarly, in the case of butterfly (Female), the nipples are regular polygons with a well-defined number of sides (5-, 6-, and 7-sided polygons) as shown in Figure 6e,f. More examples of the amorphous nature of the nipple arrangement and 5-coordinated and 7-coordinated defects and their combination along the grain boundary are shown in Figure S5 and Figure S6 in the Supporting Information, respectively. Large-area images show an extremely high density of corneal nipples with most of them having the hexagonal arrangement. One such perfect hexagonal arrangement is shown in Figure 6f where a central hexagonal pillar is surrounded with six nearest neighbors with each having 6-sides. Careful analysis of the number of nipples shows that there are about two 7-coordinated defects and one 5-coordinated defect in every square micrometer area of the facet. For example, an area of $7.5 \mu\text{m} \times 5.6 \mu\text{m}$ consists of about 70 heptagonal defects and 55 pentagonal defects.

Using the effective medium theory (EMT), we can calculate the dependency of the reflectivity with the refractive index as shown in Figure 5a. The overall reflectivity is more than that of moths around the refractive index of chitin (R.I. = 1.52). The male butterfly reflects more light compared to the female butterfly. Even though the difference in the reflectance is small, this might be sufficient to give a female butterfly advantage over a male butterfly.

(7-5) Defect Analysis. From the images analyzed for both male and female moth, we find that interwoven 5- and 7-coordinated sites to form a (7-5) defect are commonly seen in

all the samples. Figure 4 shows one such small area in the male and female moths. The otherwise perfect hexagonal arrangement is disturbed by the existence of this defect. The (7-5) defect is formed by a combination of a 5-coordinated site and a 7-coordinated site. A similar defect structure is also reported in different butterfly species.^{36,37} These defects form the demarcation between two adjacent grains of the perfect hexagonal arrangement of the corneal nipples. Even though the defects are formed by the combined 5- and 7-defects, the concentrations of isolated defect sites are very low. There are no vacancies found in all the images. Interestingly, similar kind of defects is seen in solid-state materials, which have the hexagonal symmetry. It is well known in the solid-state materials that the presence of a 5-coordinated site creates a compressive strain and a 7-coordinated site creates a tensile strain in the lattice. A proper combination of the 5- and the 7-coordinated site will cancel out the elastic strain caused. These two kinds of topological defects create grain boundaries resulting in nanoscale out-of-plane deformation. The system minimizes the energy by forming a line of such defects to form the boundary.^{39,41,45} This strain is minimized by forming a continuous (7-5) defects. As shown in Figure 4a, defects such as (7-5), (7-5-7), and (7-5-7-5) can be seen. There is no particular sequence in which the defects arise, but it is found that they define a set of misorientation. These well-defined orientations are energetically favorable. Even though the actual reason for their existence is unknown, one can presume that this might be due to the curvature of the eye and also the sub-surface structure of the eyes. Similar (7-5) defects and their combination can be seen in abundance in the case of moth (Female) as shown in Figure 4b. Across the boundary, a perfect hexagonal arrangement of the corneal nipples can be seen, which spans a region of 15–20 lattice constants across three crystallographic directions. Similar (7-5) defects and

their combination can be seen in butterflies too. Here, the corneal nipples are densely packed with the gap between the nipples of about 20–25 nm. Another important observation in the (7-5) defect is that the 5-coordinated nipple at the center is always smaller in diameter and the 7-coordinated defect is comparatively larger in size than normal corneal nipples. The average value diameter of the central pillar of the 5-coordinated site is about 120 nm, and the central pillar of the 7-coordinated site is about 160 nm. A variety of defects and defect lines observed in the case of moths and butterflies are shown in Figure S4 in the Supporting Information. Even though there are two orders of the magnitude size difference in the hexagonal lattice compared to the atomic lattices in the case of solid-state materials, it is surprising that the kind of defects that can be formed are similar. This implies that these defect locations purely originate due to the natural consequence of the hexagonal packing and the curvature of the surface.

One might wonder what is the mechanism of the growth of such regular nipple structures in the eye of moth and butterfly. Analysis of only scanning electron microscopy images of a fully grown eye will not give us a complete understanding of the process. In-depth analysis during the developmental stages of the corneal nipples is essential to identify the actual growth mode. There are two widely accepted models to understand the growth kinetics of the nipples: the microvilli model^{53,54} and the Turing model.¹³ The microvilli model suggests that the nipple arrays grow due to the diffusion of the nipple material from below the surface. This model demands that the nipple structures be uniformly distributed unless otherwise restricted by the pre-existing defect structures on the surface. The final hexagonal pattern of nipples requires a favorable initial arrangement of microvilli. One should note that this model can describe the existence of the 5- and 7-coordinated defects and the (7-5) defect as a result of some elastic strain due to the curvature. Thus, the model can be of help to understand the crystallographic structure and defect structures in the facets. The Turing model or reaction–diffusion system is based on the interaction of two chemical substances known as activator–inhibitor pair.^{13,36,55} This is a process where the competition between the synthesis–inhibition results in an oscillatory system. The material diffuses into the subsequent positions by proper selection of the catalytic constant and diffusion constant. The wavelength resulting from this process depends on these reactions and diffusion constants. This process will start nucleating multiple nipple arrays at many locations showing up as many crystalline grains. This model fits very well with nucleation in a small area. However, any acceptable model has to satisfy the large-area nucleation with multigrain structure. Meanwhile, the model satisfies the existence of individual 5- and 7-coordinated defect (for example, Hemipteran corneal nanocoatings¹³ do not specifically explain the occurrence of the (7-5) and their combination of defects forming the grain boundary in our samples. In this sense, the observed nipple pattern in a moth(Male/Female) can be an intermediate state of various Turing patterns. We have seen that the Turing patterns still does not explain the existence of polygonal shapes of the nipples and their ultra high dense packing in the case of butterfly(Male/Female). This can be understood only by an in-depth analysis of the nipple pattern during the developmental stages. Further, previous studies on the molecular origin and evolutionary diversification of the insect corneal structure based on the Turing reaction–

diffusion system suggests that there is no clear correlation between evolutionary advances of the insect group and the types of nanostructures they possess.¹³ These findings are highly significant as they support the idea that the evolutionary demands do not influence nanostructures development; however, it might be based on the functional or behavioral adaptation of insect groups. The differences in the pillar structure and area of crystalline grains between the moth and butterfly corneal nipples suggest that these changes might be due to their environmental adaptation and foraging behavior. However, it needs to be analyzed further using different groups of insects adapted to different ecological conditions.

■ CONCLUSIONS

Moth and butterfly ommatidial nanostructures have been studied by means of high-resolution electron microscopy images. The *Daphnis nerii* moth(Male/Female) shows a typical moth eye structure commonly observed. A universal (7-5) defect structure is seen with a 5-coordinated defect acting as the source of a grain boundary, which separates the regular hexagonal lattice of corneal nipples extending up to 15–20 lattice units. The average grain size in a moth(Male) is about 1.47 μm with most of the grains in between 1 and 2 μm . The average grain size in a moth(Female) is about 1.7 μm , and the majority of the grains are between 1.3 and 2.3 μm . The grains show log-normal distribution, indicating nucleation and growth mechanism. The grains also show in a definite set of misorientation with respect to each other. The *Papilio polytes* butterfly shows that the more compact arrangement of corneal nipple and individual nipple is a polygon with 5–7 sides. Even though the (7-5) defect is most commonly seen, the structure of this (7-5) defect is completely different compared to that in the moth eye. The center pillar itself is a polygon (either a 5-coordinated or 7-coordinated defect) with nearest neighbors being pentagonal and hexagonal nipples forming the (7-5) defect. The diffused Fourier transform images depict the amorphous nature of the nipple arrangement. This means that we do not see any area with a regular arrangement of nipples. This different arrangement gives a subtle difference in the reflection of the optical light between these two species. Our detailed comparison and distinction of the corneal nipple structure between moth and butterfly can pave the way to design optimized anti-reflective coating materials in the solid state.

■ EXPERIMENTAL SECTION

We used nocturnally active *Daphnis nerii* moth⁵⁶ and diurnally active *Papilio polytes* butterfly^{57,58} to compare the structural properties of corneal nipples in two species that are adapted to different environmental conditions. Eye samples from both moth and butterfly (both sexes) were passed through a series of alcohol grades (20%, 30%, 50%, 60%, 75%, 90%, and twice in 100% for 20 min each) followed by two times washing in acetone. Upon drying, the samples were mounted on carbon tape placed on an aluminum stub. The samples were then gold-coated by sputter deposition for 5 min before imaging. Samples were imaged in a Zeiss Merlin Compact VP/Zeiss Gemini scanning electron microscope (Germany). For image analysis, we used the window-based scanning probe image analysis software (WSxM 5.0).⁵⁹ The grain area calculation was done using ImageJ (<https://imagej.net/>) software. ImageJ software calculates the area of arbitrary shapes. Finally, assuming a

circular shape of the grain, the grain size (d) is calculated using the equation³⁶

$$d = \sqrt{\frac{4A}{\pi}} \quad (5)$$

■ ASSOCIATED CONTENT

SI Supporting Information

The Supporting Information is available free of charge at <https://pubs.acs.org/doi/10.1021/acsomega.0c02314>.

(Figure S1) Detailed analysis of the Fourier transform images used in Figure 3 in the manuscript, (Figure S2) Fourier transform filtered images of the moth(Male) and moth(Female) clearly indicating the various crystal grains and their angular separation, (Figure S3) grain size distribution and cumulative size distribution of the grains in moth(Male) and moth(Female), (Figure S4) comparison of the reflectance between moth and butterfly male and moth and butterfly female separately, (Figure S5) large-scale scanning electron microscopy (SEM) images and the Fourier transform filtered images for both butterfly(Male) and butterfly(Female), and (Figure S6) detailed view of 5- and 7-coordinated defects in moth(Male/Female) and butterfly(Male/Female) (PDF)

■ AUTHOR INFORMATION

Corresponding Author

R. Thamankar – Department of Physics, School of Advanced Sciences, VIT, Vellore, Tamilnadu, India 632014; orcid.org/0000-0002-1761-1970; Email: rameshm.thamankar@vit.ac.in

Author

Shamprasad Varija Raghu – Neurogenetics Lab, Dept of Applied Zoology, Mangalore University, Mangalagangothri, Karnataka, India 574199

Complete contact information is available at:

<https://pubs.acs.org/doi/10.1021/acsomega.0c02314>

Notes

The authors declare no competing financial interest.

■ ACKNOWLEDGMENTS

R.T. thanks VIT for providing “VIT SEED GRANT” for carrying out this research work. S.V.R. is supported by the DBT-Ramalingaswami Re-entry fellowship (102/IFD/SAN/1997/2015-16). Authors acknowledge Mr. Deepak Naik, Dept. of Applied Zoology, Mangalore University for providing the samples and Dr. Murari, DST-PURSE, Mangalore University for technical help in scanning electron microscopy imaging.

■ REFERENCES

(1) Prum, R. O.; Quinn, T.; Torres, R. H. Anatomically diverse butterfly scales all produce structural colours by coherent scattering. *J. Exp. Biol.* **2006**, *209*, 748–765.
(2) Wilts, B. D.; Zubiri, B. A.; Klatt, M. A.; Butz, B.; Fischer, M. G.; Kelly, S. K.; Spiecker, E.; Steiner, U.; Schröder-Turk, G. E. Butterfly gyroid nanostructures as a time-frozen glimpse of intracellular membrane development. *J. Exp. Biol.* **2017**, *3*, No. e1603119.

(3) Fu, J.; Yoon, B.-J.; Park, J. O.; Srinivasarao, M. Imaging optical scattering of butterfly wing scales with a microscope. *Interface Focus* **2017**, *7*, 20170016.

(4) Tabata, H.; Kumazawa, K.; Funakawa, M.; Takimoto, J.; Akimoto, M. Microstructures and optical properties of scales of butterfly wings. *Opt. Rev.* **1996**, *3*, 139.

(5) Stavenga, D. G.; Giraldo, M. A.; Leertouwer, H. L. Butterfly wing colors: glass scales of *graphium sarpedon* cause polarized iridescence and enhance blue/green pigment coloration of the wing membrane. *J. Exp. Biol.* **2010**, *213*, 1731–1739.

(6) Stoddart, P. R.; Cadusch, P. J.; Boyce, T. M.; Erasmus, R. M.; Comins, J. D. Optical properties of chitin: surface-enhanced raman scattering substrates based on antireflection structures on cicada wings. *Nanotechnology* **2006**, *17*, 680.

(7) Yoshida, A.; Motoyama, A.; Kosaku, A.; Miyamoto, K. Antireflective nanoprotuberance array in the transparent wing of a hawkmoth *Cephonodes hylas*. *Zool. Sci.* **1997**, *14*, 737–741.

(8) Chen, P.-J.; Awata, H.; Matsushita, A.; Yang, E.-C.; Arikawa, K. Extreme spectral richness in the eye of the common bluebottle butterfly, *graphium sarpedon*. *Front. Ecol. Evol.* **2016**, *4*, 1–12.

(9) Kelber, A.; Thunell, C.; Arikawa, K. Polarisation-dependent colour vision in papilio butterflies. *J. Exp. Biol.* **2001**, *204*, 2469–2480.

(10) Bernhard, C. G.; Gemne, G.; Sällström, J. Comparative ultrastructure of corneal surface topography in insects with aspects on phylogenesis and function. *Z. vergl. Physiol.* **1970**, *67*, 1–25.

(11) Watson, G. S.; Watson, J. A. Natural nano-structures on insects-possible functions of ordered arrays characterized by atomic force microscopy. *App. Sur. Sci.* **2004**, *235*, 139–144.

(12) Stavenga, D. G.; Foletti, S.; Palasantzas, G.; Arikawa, K. Light on the moth-eye corneal nipple array of butterflies. *Proc. R. Soc. B* **2006**, *273*, 661–667.

(13) Blagodatski, A.; Sergeev, A.; Kryuchkov, M.; Lopatina, Y.; Katanaev, V. L. Diverse set of Turing nanopatterns coat corneae across insect lineages. *Proc. Natl. Acad. Sci. U. S. A.* **2015**, *112*, 10750–10755.

(14) Bernhard, C. G.; Miller, W. H. A corneal nipple pattern in insect compound eyes. *Acta Physiol. Scand.* **1962**, *56*, 385–386.

(15) Parker, A. R.; Hegedus, Z.; Watts, R. A. Solar absorber antireflector on the eye of an eocene fly (45 Ma). *Proc. R. Soc. London B* **1998**, *265*, 811.

(16) Peisker, H.; Gorb, S. N. Always on the bright side of life: Anti-adhesive properties of insect ommatidia grating. *J. Exp. Biol.* **2013**, *213*, 3457–3462.

(17) Lin, H.; Ouyang, M.; Chen, B.; Zhu, Q.; Wu, J.; Lou, N.; Dong, L.; Wang, Z.; Fu, Y. Design and fabrication of moth-eye subwavelength structure with a waist on silicon for broadband and wide-angle anti-reflection property. *Coatings* **2018**, *8*, 360.

(18) Clapham, P. B.; Hutley, M. C. Reduction of lens reflexion by the “Moth Eye” principle. *Nature* **1973**, *244*, 281–282.

(19) Gombert, A.; Rose, K.; Heinzel, A.; Horbelt, W.; Zanke, C.; Bläsi, B.; Wittwer, V. Antireflective submicrometer surface-relief gratings for solar applications. *Sol. Energy Mater. Sol. Cells* **1998**, *54*, 333–342.

(20) Kintaka, K.; Nishii, J.; Mizutani, A.; Kikuta, H.; Nakano, H. Antireflection microstructures fabricated upon fluorine-doped SiO₂ films. *Opt. Lett.* **2001**, *26*, 1642–1644.

(21) Escoubas, L.; Simon, J. J.; Loli, M.; Berginc, G.; Flory, F.; Giovannini, H. An antireflective silicon grating working in the resonance domain for the near infrared spectral region. *Opt. Commun.* **2003**, *226*, 81–88.

(22) Kanamori, Y.; Hane, K.; Sai, H.; Yugami, H. 100 nm period silicon antireflection structures fabricated using a porous alumina membrane mask. *Appl. Phys. Lett.* **2001**, *78*, 142.

(23) Hadobás, K.; Kirsch, S.; Carl, A.; Acet, M.; Wassermann, E. F. Reflection properties of nanostructure-arrayed silicon surfaces. *Nanotechnology* **2000**, *11*, 161–164.

(24) Boden, S. A.; Bagnall, D. M. Tunable reflection minima of nanostructured antireflective surfaces. *Appl. Phys. Lett.* **2008**, *93*, 133108.

- (25) Xi, C.; Zhong-Chao, F.; Jing, Z.; Guo-Feng, S.; Liang-Hui, C. Pseudo rhombus-shaped subwavelength crossed gratings of GaAs for broadband antireflection. *Chin. Phys. Lett.* **2010**, *27*, 124210.
- (26) Boden, S. A.; Bagnall, D. M. Nanostructured biomimetic moth-eye arrays in silicon by nanoimprint lithography. In *Biomimetics and Bioinspiration*; International Society for Optics and Photonics: 2009; 7401, 74010J.
- (27) Stavroulakis, P. I.; Boden, S. A.; Johnson, T.; Bagnall, D. M. Suppression of backscattered diffraction from sub-wavelength 'moth-eye' arrays. *Opt. Express* **2013**, *21*, 1–11.
- (28) Dewan, R.; Fischer, S.; Meyer-Rochow, V. B.; Özdemir, Y.; Hamraz, S.; Knipp, D. Studying nanostructured nipple arrays of moth eye facets helps to design better thin film solar cells. *Bioinspir. Biomim.* **2012**, *7*, 016003–016011.
- (29) Han, Z.; Jiao, Z.; Niu, S.; Ren, L. Ascendant bioinspired antireflective materials: Opportunities and challenges coexist. *Prog. Mater. Sci.* **2019**, *103*, 1–68.
- (30) Rahman, A.; Ashraf, A.; Xin, H.; Tong, X.; Sutter, P.; Eisaman, M. D.; Black, C. T. Sub-50-nm self-assembled nanotextures for enhanced broadband antireflection in silicon solar cells. *Nat. Commun.* **2015**, *6*, 5963.
- (31) Sai, H.; Kanamori, Y.; Arafune, K.; Ohshita, Y.; Yamaguchi, M. Light trapping effect of submicron surface textures in crystalline Si solar cells. *Progr. Photovolt.: Res. Appl.* **2007**, *15*, 415–423.
- (32) Han, K.-S.; Shin, J.-H.; Yoon, W.-Y.; Lee, H. Enhanced performance of solar cells with anti-reflection layer fabricated by nano-imprint lithography. *Sol. Energy Mater. Sol. Cells* **2011**, *95*, 288–291.
- (33) Kim, J.-J.; Lee, Y.; Kim, H. G.; Choi, K.-J.; Kweon, H.-S.; Park, S.; Jeong, K.-H. Biologically inspired LED lens from cuticular nanostructures of firefly lantern. *Proc. Natl. Acad. Sci. U. S. A.* **2012**, *109*, 18674–18678.
- (34) Park, G. C.; Song, Y. M.; Ha, J.-H.; Lee, Y. T. Broadband antireflective glasses with subwavelength structures using randomly distributed Ag nanoparticles. *J. Nanosci. Nanotechnol.* **2011**, *11*, 6152–6156.
- (35) Lee, K. C.; Erb, U. Grain boundaries and coincidence site lattices in the corneal nanonipple structure of the Mourning Cloak butterfly. *Beilstein J. Nanotechnol.* **2013**, *4*, 292–299.
- (36) Lee, K. C.; Yu, Q.; Erb, U. Mesostucture of ordered corneal nano-nipple arrays: The Role of 5-7 coordination Defects. *Sci. Rep.* **2016**, *6*, 28342–28353.
- (37) Lee, K. C.; Erb, U. Remarkable crystal and defect structures in butterfly eye nano-nipple arrays. *Arthropod Struct. Dev.* **2015**, *44*, 587–594.
- (38) Spalding, A.; Shanks, K.; Bennie, J.; Potter, U.; French-Constant, R. Optical modelling and phylogenetic analysis provide clues to the likely function of corneal nipple arrays in butterflies and moths. *Insects* **2019**, *10*, 262.
- (39) Zhang, X.; Xu, Z.; Yuan, Q.; Xin, J.; Ding, F. The favourable large misorientation angle grain boundaries in graphene. *Nanoscale* **2015**, *7*, 20082–20088.
- (40) Liu, Y.; Jakobson, B. I. Cones, pringles and grain boundary landscapes in graphene topology. *Nano Lett.* **2010**, *10*, 2178–2183.
- (41) Yazyev, O. V.; Louie, S. G. Topological defects in graphene: Dislocations and grain boundaries. *Phys. Rev. B* **2010**, *81*, 195420–195427.
- (42) Liu, Y.; Zou, X.; Jakobson, B. I. Dislocations and grain boundaries in two-dimensional boron nitride. *ACS Nano* **2012**, *6*, 7053–7058.
- (43) Roshal, D. S.; Petrov, Y. K.; Myasnikova, A. E.; Rochal, S. B. Extended topological defects as sources and outlets of dislocations in spherical hexagonal crystals. *Phys. Lett. A* **2014**, *378*, 1548–1552.
- (44) Cretu, O.; Lin, Y. C.; Suenaga, K. Evidence for active atomic defects in monolayer hexagonal boron nitride: A new mechanism of plasticity in two-dimensional materials. *Nano Lett.* **2014**, *14*, 1064–1068.
- (45) Hashimoto, A.; Suenaga, K.; Gloter, A.; Urita, K.; Iijima, S. Direct evidence for atomic defects in graphene layers. *Nature* **2004**, *430*, 870–873.
- (46) Han, J.; Vitek, V.; Srolovitz, D. J. The grain-boundary structural unit model redux. *Acta Mater.* **2017**, *133*, 186–199.
- (47) Weins, M.; Gleiter, H.; Chalmers, B. Structure of symmetric tilt boundaries. *Scr. Metall.* **1970**, *4*, 235–238.
- (48) Abbaschian, R.; Abbaschian, L.; Reed-Hill, R. E. *Physical Metallurgy Principles*; CENGAGE Learning: U.S.A., 2009.
- (49) Kuo, W.-K.; Hsu, J.-J.; Nien, C.-K.; Yu, H.-H. Moth-eye-inspired biophotonic surfaces with antireflective and hydrophobic characteristics. *ACS Appl. Mater. Interfaces* **2016**, *8*, 32021–32030.
- (50) Nakata, K.; Sakai, M.; Ochiai, T.; Murakami, T.; Takagi, K.; Fujishima, A. Antireflection and self-cleaning properties of a moth-eye like surface coated with TiO₂ particles. *Langmuir* **2011**, *27*, 3275–3278.
- (51) Sun, J.; Wang, X.; Wu, J.; Jiang, C.; Shen, J.; Cooper, M. A.; Zheng, X.; Liu, Y.; Yang, Z.; Wu, D. Biomimetic moth-eye nanofabrication: Enhanced antireflection with superior self-cleaning characteristic. *Sci. Rep.* **2018**, *8*, 5438–5448.
- (52) Ji, S.; Song, K.; Nguyen, T. B.; Kim, N.; Lim, H. Optimal moth-eye nanostructure array on transparent glass towards broadband antireflection. *ACS Appl. Mater. Interfaces* **2013**, *5*, 10731–10737.
- (53) Fröhlich, A. A scanning electron-microscopic study of apical contacts in the eye during postembryonic development of *Drosophila melanogaster*. *Cell Tissue Res.* **2001**, *303*, 117–128.
- (54) Gemne, G. Ontogenesis of corneal surface ultrastructure in nocturnal lepidoptera. *Philos. Trans. R. Soc. London B. Biol. Sci.* **1971**, *262*, 343–363.
- (55) Meinhardt, H. *Models of biological pattern formation*; Academic Press Inc: London, 1982.
- (56) Sant, H. H.; Sane, S. P. The mechanosensory-motor apparatus of antennae in the oleander hawk moth (*Daphnis nerii*, Lepidoptera). *J. Comp. Neurol.* **2018**, *526*, 2215–2230.
- (57) Iijima, T.; Yoda, S.; Fujiwara, H. The mimetic wing pattern of *Papilio polytes* butterflies is regulated by a doublesex-orchestrated gene network. *Biol.* **2019**, *2*, 257–267.
- (58) Nishikawa, H.; Iga, M.; Yamaguchi, J.; Saito, K.; Kataoka, H.; Suzuki, Y.; Sugano, S.; Fujiwara, H. Molecular basis of wing coloration in a Batesian mimic butterfly, *Papilio polytes*. *Sci. Rep.* **2013**, *3*, 3184–3193.
- (59) Horcas, I.; Fernández, R.; Gómez-Rodríguez, J. M.; Colchero, J.; Gómez-Herrero, J.; Baro, A. M. WSxM: A software for scanning probe microscopy and a tool for nanotechnology. *Rev. Sci. Instrum.* **2007**, *78*, No. 013705.